Kelvin-Helmholtz instabilities at the magnetic cavity boundary of comet 67P/Churyumov-Gerasimenko

M. Rubin,[1] K. C. Hansen,[1] M. R. Combi,[1] L. K. S. Daldorff,[1] T. I. Gombosi,[1] and V. M. Tenishev[1]

Received 25 October 2011; revised 30 April 2012; accepted 1 May 2012; published 27 June 2012.

[1] We investigate the plasma environment of comet 67P/Churyumov-Gerasimenko, the target of the European Space Agency's Rosetta mission. Rosetta will rendezvous with the comet in 2014 at almost 3.5 AU and follow it all the way to and past perihelion at 1.3 AU. During its journey towards the inner solar system the comet's environment will significantly change. The interaction of the solar wind with a well developed neutral coma leads to the formation of an upstream bow shock and, closer to the comet, the inner shock separating the solar wind, with cometary pick-up ions mass-loaded, from the inner cometary ions which are dragged outward through abundant collisions and charge exchange with the expanding neutral gas. As a consequence the interplanetary magnetic field is prevented from penetrating the innermost region of the comet, the so-called magnetic cavity. We use our magnetohydrodynamics model BATSRUS (Block-Adaptive-Tree-Solarwind-Roe-Upwind-Scheme) to simulate the solar wind – comet interaction. The model includes photoionization, ion-electron recombination, and charge exchange. Under certain conditions our model predicts an unstable plasma flow at the inner shock. We show that the plasma shear flow around the magnetic cavity can lead to Kelvin-Helmholtz instabilities. We investigate the onset of this phenomenon with change of heliocentric distance and furthermore show that a previously stable magnetic cavity boundary can become unstable when the neutral gas is predominately released from the dayside of the comet.

Citation: Rubin, M., K. C. Hansen, M. R. Combi, L. K. S. Daldorff, T. I. Gombosi, and V. M. Tenishev (2012), Kelvin-Helmholtz instabilities at the magnetic cavity boundary of comet 67P/Churyumov-Gerasimenko, *J. Geophys. Res.*, *117*, A06227, doi:10.1029/2011JA017300.

1. Introduction

[2] On March 14, 1986 the European Space Agency's Giotto spacecraft flew-by comet 1P/Halley. One of the main results of the mission was the discovery of the magnetic field-free cavity. The Giotto magnetometer observed a very sharp decrease of the magnetic field strength along its trajectory at roughly 4500 km from the nucleus [*Neubauer et al.*, 1986]. The magnetic cavity boundary (i.e. contact surface, ionopause) separates the magnetized from the unmagnetized cometary plasma [*Cravens*, 1989a]. Various studies [e.g., *Schmidt et al.*, 1986; *Ip and Axford*, 1987; *Sauer and Baumgaertel*, 1986; *Eviatar and Goldstein*, 1988; *Benna and Mahaffy*, 2007] of this boundary revealed it to be the consequence of a tight interplay between the out-flowing supersonic neutral gas and the outflowing plasma through ion-neutral friction preventing the subsonic, magnetized cometary plasma from entering the cavity region. The boundary is located where this outward pointed ion-neutral drag force equals the magnetic pressure gradient force and the magnetic curvature force ($\vec{\mathbf{j}} \times \vec{\mathbf{B}}$) as discussed by *Cravens* [1987]. On the sunward side of this boundary the magnetic field is piled-up and draped around the magnetic cavity. Further away from the comet the collisionopause or cometopause is located where cometary ions dominate the plasma density over the solar wind proton density and separates the collisionless solar wind plasma flow from the cometary gas. Even farther upstream, the bow shock is located where the solar wind is decelerated from supersonic to subsonic speeds.

[3] Our global model of the comet – solar wind interaction [*Rubin et al.*, 2009], originally developed by *Gombosi et al.* [1996] for comet 1P/Halley, has previously been used to discuss the complex ion-neutral chemistry through in depth comparison with the measurements obtained by Giotto's Ion Mass Spectrometer [*Balsiger et al.*, 1986]. The Block Adaptive Tree Solar-wind Roe-type Upwind Scheme (BATSRUS) solves the governing equations of magnetohydrodynamics [*Tóth et al.*, 2005] accounting for photoionization, recombination, and ion-neutral frictional drag in an adaptive unstructured Cartesian mesh. Such an approach

[1]Department of Atmospheric, Oceanic and Space Sciences, University of Michigan, Ann Arbor, Michigan, USA.

Corresponding author: M. Rubin, Department of Atmospheric, Oceanic and Space Sciences, University of Michigan, 2455 Hayward St., Ann Arbor, MI 48109, USA. (rubinmar@umich.edu)

0148-0227/12/2011JA017300

allows the model to resolve the various features of the comet involving very different length scales.

[4] In this work we focus on the plasma environment of comet 67P/Churyumov-Gerasimenko the target of the European Space Agency's Rosetta mission. After the rendezvous with the comet the Rosetta spacecraft will accompany 67P/Churyumov-Gerasimenko from almost 3.5 AU all the way to and past perihelion at 1.3 AU. *Benna and Mahaffy* [2006] extrapolated results from their model of comet 26P/Grigg-Skjellerup to comet 67P/Churyumov-Gerasimenko to derive the expected plasma environment at perihelion. Model predictions for the comet's plasma environment in the whole range of heliocentric distances relevant for Rosetta have been presented by *Gortsas et al.* [2010], *Motschmann and Kührt* [2006], and *Hansen et al.* [2007].

[5] While many models use symmetric gas production profiles, asymmetric neutral gas distributions of comet 67P/Churyumov-Gerasimenko have been investigated by *Wiehle et al.* [2011] applying hybrid techniques and for comet 19P/Borrelly by *Jia et al.* [2008] using the BATS-RUS model. *Schleicher et al.* [2003], however, reported from observations that the neutral gas distribution during the flyby of the Deep Space 1 spacecraft at comet 19P/Borrelly was rather symmetric with respect to the sun-comet line. Therefore, to reproduce the observed asymmetries in the plasma boundaries by the Deep Space 1 spacecraft *Delamere* [2006] investigated the effect of the finite ion gyroradius applying a hybrid model to the solar wind interaction with comet 19P/Borrelly. Nevertheless, asymmetric neutral gas production rates will affect the ion-neutral drag force that is balanced by the magnetic pressure gradient force and the magnetic curvature force at the location of the cavity boundary. At larger heliocentric distances, where the strength of the interplanetary magnetic field and the magnetic pressure gradient force decrease, the distribution of active regions over the comet's surface may more strongly influence the shape of the magnetic cavity. This is especially interesting as the geometry of the cavity influences the topology of the plasma streamlines crossing the shock. These jump-conditions can be derived by integrating the magnetohydrodynamics (MHD) equations across the shock and are called Rankine-Hugoniot equations for MHD [see, e.g., *Draine and McKee*, 1993]. We will show that the tailward plasma flow can be significantly altered and then concentrated in the plane perpendicular to the Interplanetary Magnetic Field (IMF), a phenomenon that might be observable by Rosetta.

[6] Kelvin-Helmholtz instabilities have been observed and predicted in various environments including among others cometary tails [*Ershkovich*, 1980], Venus [*Wolff et al.*, 1980; *Möstl et al.*, 2011], Mercury [*Boardsen et al.*, 2010], Saturn [*Pu and Kivelson*, 1984; *Masters et al.*, 2009; *Delamere et al.*, 2011], and Pluto where *Delamere* [2009] reported a Kelvin-Helmholtz unstable heavy ion discontinuity. Here, in the case of the comet's magnetic cavity boundary [see also *Ershkovich et al.*, 1986; *Chen and Liu*, 1992], we will show that, depending on the asymmetry of the neutral gas distribution and the strength of the magnetic field, the plasma flow around the cavity boundary can become unstable due to the formation of Kelvin-Helmholtz instabilities.

2. The Model

[7] We use the BATSRUS model as part of the Space Weather Modeling Framework [see *Tóth et al.*, 2005] to solve the single fluid ideal MHD equations applied to cometary comae. The computational domain ranges from $\pm 4 \cdot 10^6$ km along the Sun-comet axis and $\pm 2 \cdot 10^6$ km in both perpendicular directions to properly accommodate the physical scales required to simulate the gradual mass loading of the solar wind upstream of the bow shock. At the other extreme of the length scale, the model's resolution reaches less than 1 km at the location of the nucleus.

[8] The conservative form of the MHD equations, when neglecting terms including gravity and the low neutral gas temperature is:

$$\frac{\partial}{\partial t}\begin{pmatrix} \rho \\ \rho\vec{\mathbf{u}} \\ \vec{\mathbf{B}} \\ E \end{pmatrix} + \nabla \begin{pmatrix} \rho\vec{\mathbf{u}} \\ \rho\vec{\mathbf{u}}\vec{\mathbf{u}} + \left(p + \frac{1}{2\mu_0}B^2\right)\vec{\mathbf{I}} - \frac{\vec{\mathbf{B}}\vec{\mathbf{B}}}{\mu_0} \\ \vec{\mathbf{u}}\vec{\mathbf{B}} - \vec{\mathbf{B}}\vec{\mathbf{u}} \\ \frac{1}{2}\rho u^2 + \frac{\gamma}{\gamma-1}p\vec{\mathbf{u}} + \frac{(\vec{\mathbf{B}}\cdot\vec{\mathbf{B}})\vec{\mathbf{u}} - \vec{\mathbf{B}}(\vec{\mathbf{B}}\cdot\vec{\mathbf{u}})}{\mu_0} \end{pmatrix} = \vec{\mathbf{S}} \tag{1}$$

where $\vec{\mathbf{I}}$ is a 3×3 unit matrix. On the right hand side the source term $\vec{\mathbf{S}}$ can be written as:
with m_i the mean ion mass, n_i the ion number density, ρ_i the ion mass density, n_n the neutral number density, ν_n the ionization frequency, $\vec{\mathbf{u}}_n$ the neutral velocity, k_{in} the ion-neutral collision momentum-energy transfer rate per unit volume including elastic and inelastic collisions (set to $1.7 \cdot 10^{-9}$ cm^3s^{-1} as in *Gombosi et al.* [1996]), α_i is the recombination rate, n_e the electron number density (assumed to be equal to n_i), and γ the adiabatic index (set to $\frac{5}{3}$). The values for the solar wind conditions used can be found in Table 1. We use the recombination rate from *Eberhardt and Krankowsky* [1995] as done in *Gombosi et al.* [1996]

$$\vec{\mathbf{S}} = \begin{pmatrix} \nu_n n_n - \alpha_i n_e n_i \\ (\nu_n n_n + k_{in} n_n n_i)(\vec{\mathbf{u}}_n - \vec{\mathbf{u}}) \\ 0 \\ \frac{1}{2}\left(m_i n_n \nu_n u_n^2 - \rho_i \alpha_i n_e u^2 + \rho_i k_{in} n_n (u_n^2 - u^2)\right) - \frac{1}{\gamma-1}p(k_{in} n_n + \alpha_i n_i) \end{pmatrix} \tag{2}$$

$$\alpha_i(T_e) = \begin{cases} \alpha_0 \sqrt{\frac{300}{T_e}} & T_e \le 200K \\ 2.342\alpha_0 T_e^{0.2553 - 0.1633\log(T_e)} & T_e > 200K \end{cases} \tag{3}$$

with $\alpha_0 = 7.0 \cdot 10^{-7}$ cm^3s^{-1} and T_e the electron temperature.

Table 1. Boundary Conditions[a]

r_H (AU)	n_{SW} (cm^{-3})	T_{SW} (K)	$\|B\|_{SW}$ (nT)	$B\measuredangle$ (deg)	λ (km)
1.3	6.0	$1.3\cdot10^5$	4.9	52	$1.7\cdot10^6$
2.0	2.5	$1.0\cdot10^5$	2.8	63	$4.0\cdot10^6$
2.7	1.4	$9.2\cdot10^4$	2.0	70	$7.3\cdot10^6$
3.0	1.1	$8.8\cdot10^4$	1.8	71	$9.0\cdot10^6$
3.3	0.9	$8.4\cdot10^4$	1.6	73	$1.1\cdot10^7$

[a]The input parameters are scaled from the following parameters at 1 AU according to *Hansen et al.* [2007]: solar wind density n_0 = 10 cm^{-3}, solar wind temperature $T_i = 5\cdot10^4$ K, photo-ionization scale length $\lambda = 10^6$ km, and the magnetic field strength |B| = 7 nT on the Parker spiral. The solar wind velocity is assumed to be $\vec{u}_{SW} = (-400, 0, 0)$ km s^{-1}. The neutral gas is assumed to outflow radially from the nucleus at a velocity of 1 km s^{-1}. We also investigated different mean ion masses of 35 amu and 17 amu to model carbon monoxide and carbon dioxide, CO/CO_2, as well as water, H_2O, dominated comets, respectively. The production rate of the symmetric component is set to $1.5\cdot10^{27}$ s^{-1} and the asymmetric component is linearly increased to the same production rate over a time-span of three minutes.

[9] We use a second order (in space as well as in time) parallel scheme to solve the consequent system of eight scalar partial differential equations, including mass density, momentum, energy, as well as magnetic field as shown in equation (1). The scheme is based on a HLLE-type Riemann-solver developed by *Linde* [1998] with a minmod type limiter. The condition $\nabla \cdot \vec{\mathbf{B}} = \mathbf{0}$ is enforced everywhere at all times using the 8-wave scheme of *Powell et al.* [1999].

[10] Although the model is capable of resolving the nucleus itself, for the sake of computational resources we neglect the influence of the physical nucleus and approximated the comet as a point source located in the center of the domain. In order to investigate the influence of an asymmetric gas production rate on the magnetic cavity boundary we use a simple analytic expression to calculate the neutral density n_n. Although BATSRUS allows a self-consistent, fully-coupled hydrodynamics description of the neutral gas phase, an analytic model simplifies the parameter study and reduces the computational requirements significantly. Our neutral distribution is given by:

$$n_n(\vec{\mathbf{r}}) = \frac{Q}{4\pi u_n |\vec{\mathbf{r}}|^2} e^{-\frac{|\vec{\mathbf{r}}| v_n}{u_n}} \cdot \begin{cases} [1 + 3 \cdot f \cdot (\cos(2\Theta) + 1)] & \text{if } 0 \le \Theta \le \frac{\pi}{2} \\ 1 & \text{if } \frac{\pi}{2} \le \Theta \le \pi \end{cases} \quad (4)$$

with Θ the angle between the surface normal of the active area $\vec{\mathbf{x}}$ and the location $\vec{\mathbf{r}}$ that can be calculated from the scalar product of both vectors

$$\Theta = a\cos\left(\frac{\vec{\mathbf{r}} \cdot \vec{\mathbf{x}}}{|\vec{\mathbf{r}}||\vec{\mathbf{x}}|}\right). \quad (5)$$

[11] Therefore the neutral gas distribution consists of a spherically symmetric component with a production rate Q and a directed component with production rate Q times the scalar f. The directed component relative to $\vec{\mathbf{x}}$ (e.g., a day and nightside asymmetry with $\vec{\mathbf{x}}$ along the Sun-comet line) follows a (cos(2Θ) + 1) profile. We previously have used a cos(Θ) profile equivalent to the solar illumination on the dayside that produces very similar results but has a jump in the first derivation at $\Theta = \frac{\pi}{2}$. Therefore, to rule out any effects of such a sharp change in the neutral gas distribution we will focus on the model presented in equation (4). The coefficient 3 comes from the normalization of this specific profile and therefore the total production rate is

$$Q_{tot} = Q \cdot (1 + f). \quad (6)$$

[12] The choice of f thus adjusts the strength of the asymmetric component. If its value is kept constant, the neutral background (symmetric and asymmetric) remains unchanged for the whole simulation.

[13] If we want to change the asymmetric component in time, i.e. as a crude approximation for a jet or an outburst from the comet's surface or just an asymmetric production rate related to the solar illumination, the neutral gas expansion velocity needs to be taken into account. The expanding neutral gas reaches locations of different cometocentric distances at distinct times. Assuming a constant neutral gas outflow velocity u_n we use the following simple model for the value of f:

$$f(\vec{\mathbf{r}}, T_{sim}) = \begin{cases} f_{start} & \text{if } \frac{|\vec{\mathbf{r}}|}{u_n} > (T_{sim} - T_{start}) \\ \frac{f_{end} - f_{start}}{T_{end} - T_{start}} \cdot (T_{sim} - T_{start}) + f_{start} & \text{if } (T_{sim} - T_{start}) \ge |\frac{|\vec{\mathbf{r}}|}{u_n} > (T_{sim} - T_{end}) \\ f_{end} & \text{if } \frac{|\vec{\mathbf{r}}|}{u_n} \le (T_{sim} - T_{end}) \end{cases} \quad (7)$$

with f_{start} and f_{end} the initial and final strength of the asymmetry, respectively. T_{sim} stands for the elapsed simulation time. T_{start} and T_{end} stand for the start and end times of the transition of the asymmetric part of the neutral gas production rate. In this simple model we therefore assume a linear transition in strength of the asymmetric production within the time-interval from T_{start} to T_{end}. Depending on the location $\vec{\mathbf{r}}$, the simulation time T_{sim}, and the neutral gas velocity u_n the value of f changes as the asymmetry propagates through the simulation domain. An example of a fully propagated jet case ($T_{sim} = \infty$) with an asymmetric component of the same strength as the symmetric component (f = 1) can be seen in Figure 1. Plotted is the relative number density of neutrals with respect to the angle from the jet center.

[14] The mass loading of the comet can also be influenced by the composition of the neutral gas (see, e.g., the model by *De Sanctis et al.* [2010]). Depending on the heliocentric distance, the abundance of water to carbon monoxide varies due to the different sublimation temperatures. We tried both, a water dominated as well as a carbon monoxide/carbon dioxide dominated environment in our model. For this purpose we either used a mean ion mass of 17 amu or 35 amu in our mass loading terms but, for the sake of simplicity, left

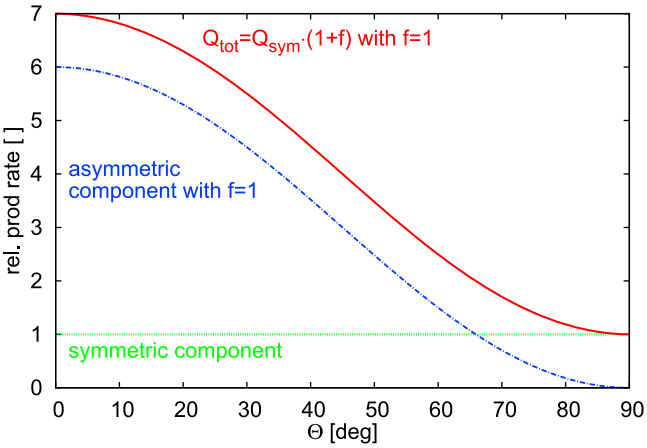

Figure 1. Relative distribution of the neutral gas with respect to the jet center. An asymmetric neutral profile of strength f can be added on top of the symmetric component. Depending on the distance from the comet the strength of the asymmetric component is adjusted according to equation (7) to account for the neutral outflow velocity.

the recombination rate, the ion-neutral friction coefficient as well as the neutral outflow velocity the same.

[15] As discussed in *Cravens* [1989a, 1989b], the magnetic cavity boundary forms where the outward ion-neutral friction force balances the inward-directed magnetic pressure gradient force and the magnetic curvature force (or $\vec{\mathbf{j}} \times \vec{\mathbf{B}}$ force) as shown in Figure 2. This requires a minimal neutral gas production rate for a magnetic cavity to form and as a consequence the upstream plasma, carrying the solar wind's magnetic field, is prevented from penetrating into the cavity. This balance is responsible for the drop in magnetic field strength close to the comet as observed by the Gotto spacecraft during the flyby at comet 1P/Halley [*Neubauer et al.*, 1986]. Theoretical studies by *Wu* [1987], including global MHD models by *Schmidt et al.* [1986], have found that the diamagnetic cavity is tear-drop shaped and is elongated in the direction of the tail. The upstream plasma flow is diverged around the magnetic cavity. In this region the ion temperature increases because of the still abundant ion-neutral interaction.

[16] For the investigation of the plasma flow across the magnetic cavity boundary we briefly discuss the jump conditions at this shock. From the Rankine-Hugoniot equations for ideal MHD follows the coplanarity relation of the magnetic field $\vec{\mathbf{B}}_{tan}$ as well as the velocity $\vec{\mathbf{u}}_{tan}$ components parallel to the shock [*Gombosi*, 2004]:

$$\left[u_{norm}\vec{\mathbf{B}}_{tan}\right] - \frac{B_{norm}^2}{\Phi_m \mu_0}\left[\vec{\mathbf{B}}_{tan}\right] = 0 \tag{8}$$

The square brackets denote the difference of the upstream and the downstream conditions across the shock with $[\vec{\mathbf{B}}] = \vec{\mathbf{B}}_{down} - \vec{\mathbf{B}}_{up}$ and the subscripts *norm* and *tan* represent the vectorial components perpendicular and tangential to the shock, respectively. The total mass flux across the shock $\Phi_m = \rho_{m_{up}}\left|\vec{\mathbf{u}}_{norm_{up}}\right| = \rho_{m_{down}}\left|\vec{\mathbf{u}}_{norm_{down}}\right|$ is conserved (ρ_m mass density). The magnetic field can thus change its magnitude across the shock but not its direction. The same applies to the velocity vector when considering

$$\left[\vec{\mathbf{u}}_{tan}\right] - \frac{B_{norm}}{\Phi_m \mu_0}\left[\vec{\mathbf{B}}_{tan}\right] = 0, \tag{9}$$

also derived from the same equations. Therefore the velocity component parallel to the shock cannot flip sign and has to bend away from the shock normal.

[17] Kelvin-Helmholtz instabilities can form in the presence of velocity shear between two different layers of fluids or plasmas [*Chandrasekhar*, 1961]. In the case of comets *Ershkovich* [1980] predicted the formation of Kelvin-Helmholtz instabilities in the tail. Here we list the condition from *Masters et al.* [2009] [see also *Ogilvie and Fitzenreiter*, 1989; *Kivelson and Pu*, 1984] for the formation of the Kelvin-Helmholtz instability in regions of strong shear flows in an incompressible plasma:

$$\left[\vec{\mathbf{k}} \cdot \left(\vec{\mathbf{V}}_2 - \vec{\mathbf{V}}_1\right)\right]^2 > \frac{1}{\mu_0} \cdot \left(\frac{1}{\rho_1} + \frac{1}{\rho_2}\right) \cdot \left[\left(\vec{\mathbf{k}} \cdot \vec{\mathbf{B}}_1\right)^2 + \left(\vec{\mathbf{k}} \cdot \vec{\mathbf{B}}_2\right)^2\right] \tag{10}$$

with $\vec{\mathbf{k}}$ the wave vector, $\vec{\mathbf{B}}_1$ and $\vec{\mathbf{B}}_2$ the magnetic fields in the bounding plasmas and the $\vec{\mathbf{V}}_1$ and $\vec{\mathbf{V}}_2$ the corresponding flow velocities. μ_0 is the permeability of free space and ρ_1 and ρ_2 stand for the two mass densities, respectively. This instability condition is derived from the dispersion equation

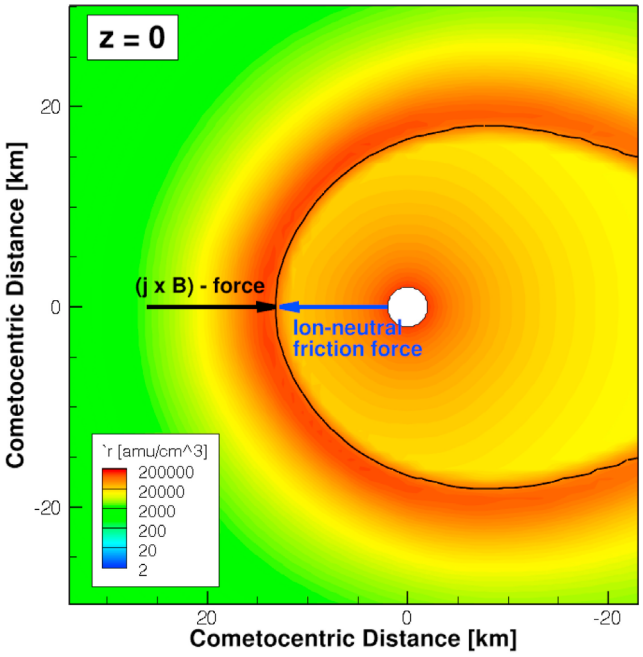

Figure 2. The magnetic cavity boundary forms where the ion-neutral friction force balances the magnetic pressure gradient force and the magnetic curvature force. The figure has been overlaid by a sphere with 2 km radius representing the comet for comparison. The Sun is on the left hand side. Plotted is the plasma mass density. For the corresponding magnetic field see Figure 4. The black contour line denotes the location of the inner shock where the plasma bulk velocity transitions from supersonic to subsonic speeds.

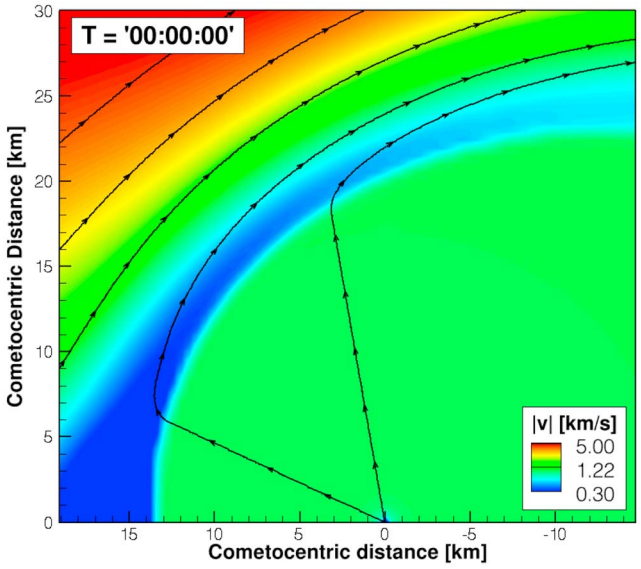

Figure 3. Plotted is the plasma bulk flow velocity (and streamlines) with the Sun on the left hand side and the comet centered at the origin. While inside the magnetic cavity the plasma flow is dominated by collisions with the abundant neutrals flowing out radially, just outside of the magnetic cavity the plasma is bent tailward and its flow velocity parallel to the shock increases.

between two adjacent sheering layers neglecting the comet's gravity. A much more rigorous discussion can be found in *Goedbloed et al.* [2010]. The Kelvin-Helmholtz instability condition here relates the plasma shear flow with the magnetic field strength as well as the plasma mass densities. When neglecting gravity at the comet it is the magnetic field that restrains the formation of the Kelvin-Helmholtz instabilities. When dividing equation (10) by $\left|\vec{\mathbf{k}}\right|^2$ and moving the terms to the right hand side the following condition can be derived for the development of the Kelvin-Helmholtz instability:

$$0 > \frac{1}{\mu_0}\cdot\left(\frac{1}{\rho_1}+\frac{1}{\rho_2}\right)\cdot\left[\left(\frac{\vec{\mathbf{k}}}{\left|\vec{\mathbf{k}}\right|}\cdot\vec{\mathbf{B}}_1\right)^2+\left(\frac{\vec{\mathbf{k}}}{\left|\vec{\mathbf{k}}\right|}\cdot\vec{\mathbf{B}}_2\right)^2\right] - \left[\frac{\vec{\mathbf{k}}}{\left|\vec{\mathbf{k}}\right|}\cdot\left(\vec{\mathbf{V}}_2-\vec{\mathbf{V}}_1\right)\right]^2. \quad (11)$$

As mentioned above the criterion presented here is based upon the assumption of incompressibility of the plasma and as such applicable only when the plasma beta, which denotes the ratio of the thermal to the magnetic pressure, is much larger than unity [*Pu and Kivelson*, 1983].

3. Results

3.1. Symmetric Neutral Gas Production

[18] We first investigate the stability of the magnetic cavity boundary for different heliocentric distances. The cometary gas production rate is symmetric and is held constant (Q_{sym} = $1.5\cdot10^{27}$ s^{-1}) by setting f to zero. Only the upstream solar wind conditions are varied according to Table 1. Obviously the production rate of the comet will change over the span of heliocentric distances covered in this work, however, here we only vary the upstream boundary conditions including the solar wind density and temperature, the magnetic field strength and the Parker spiral angle, and the solar photoionization rates.

[19] Figure 3 shows that shear flow can be observed where the upstream mass loaded plasma is forced around the magnetic cavity. This shear flow can develop Kelvin-Helmholtz instabilities as outlined in equation (10). This equation also outlines the reason for this behavior. In our model the magnetic field of the assumed Parker spiral decreases with increasing heliocentric distance. Therefore a magnetic cavity stable at small heliocentric distances can become unstable at large heliocentric distances. This effect is somewhat compensated by the simultaneous decrease of the solar photoionization frequency that decreases with heliocentric distance and thus affects the local mass loading. Nevertheless, since our simulation domain spans several million kilometers the total mass loading remains similar for the upstream mass loaded streamlines. The streamlines originating from the comet, however, are less mass loaded the larger the heliocentric distance. As both the upstream solar magnetic field as well as the solar photoionization frequency are decreasing with heliocentric distance in our model ($\sim 1/r_H^2$) and the neutral gas production rate is kept constant, the location of the magnetic cavity boundary remains at roughly 50 km for most of the shown cases.

[20] The plates in Figure 4 (left) show the magnetic field and the mass density distribution for the 2.7 AU case in the plane containing the magnetic field for a spherically symmetric neutral gas production. The Sun is on the left hand side and the magnetic field is almost symmetrically draped around the cavity as can be seen in the bottom plate. Furthermore, plotted in the top plate are the plasma streamlines, in particular also across the shock. As shown in equation (9) the plasma streamlines are bent away from the shock normal and are thus pointed tailward. The two plates on the right hand side will be discussed later.

[21] In numerical MHD models, shocks typically have a width of two to three computational cells. Therefore the result of our model depends on the chosen resolution of the simulation mesh. If the cell resolution is increased, shocks become thinner and the modeled mass density increases. This can influence the initiation of the Kelvin-Helmholtz instability as the increased mass density lowers the stabilizing effect of the magnetic field (see equation (11)). We initiated the formation of the Kelvin-Helmholtz waves by increasing the resolution on the fly and thus turning the previously steady-state solution unstable (i.e. we changed the cell resolution at the cavity boundary of the here shown 2.7 AU case from 1 km to 500 m). This is obviously a non-physical process but computationally much less expensive than modeling the required real-time on the comet's orbit with a high enough time-resolution to appropriately catch the onset of the instability on the comet's outbound path or the instability disappearing on the inbound path towards larger magnetic fields. Nevertheless this raises some questions about the applicability of the model and the validity of some key assumptions of the MHD approach. The fluid description of the plasma makes several assumptions about the plasma properties that might not be fulfilled at the shock

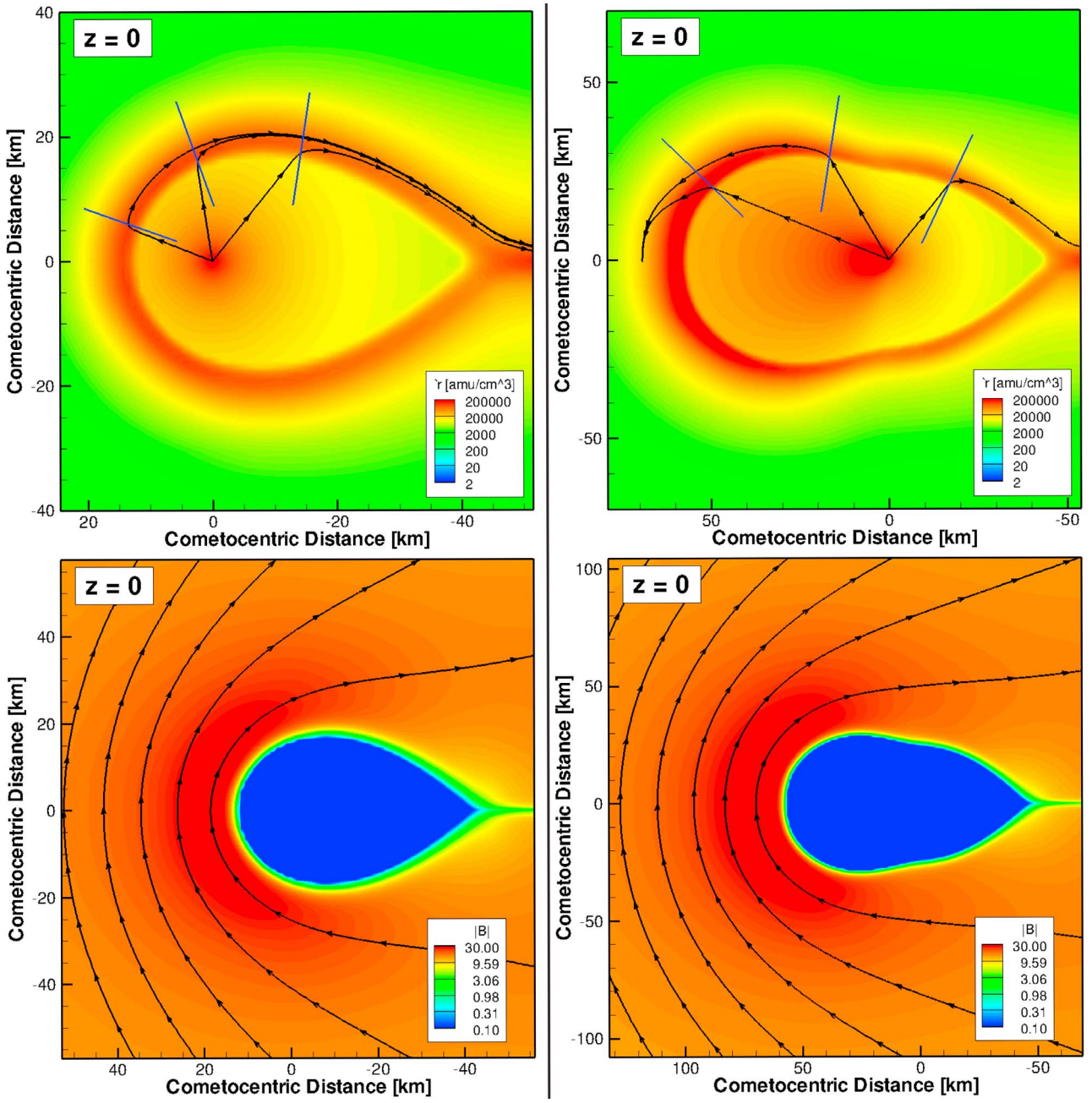

Figure 4. (top) Bending of the plasma streamlines at the inner shock in the case of a (left) symmetric neutral gas production rate and with an additional (right) sub-solar directed component plotted in the plane containing the undisturbed upstream magnetic field. The comet is located at (0, 0) and the Sun on the left. Shown are plasma mass density and bulk flow streamlines. Blue lines show the shock normal directions to illustrate the impact of equation (9) from section 2. (bottom) The associated magnetic field lines and strengths. The magnetic field-free region is clearly visible. The plotted length scales are different for the shown cases given the different extensions of the cavities in both cases.

in particular. For instance the MHD description neglects the effect of finite gyroradii, which become particularly important for low gas production rate comets as shown by *Hansen et al.* [2007], who investigated the plasma environment of comet 67P/Churyumov-Gerasimenko using both a hybrid kinetic model and our magnetohydrodynamics model BATSRUS, respectively. In Figure 5 we plotted several quantities addressing these concerns. The top left plate shows the ratio of the collision rate to the Larmor frequency. Close to the nucleus, even though the gyration radius is large, the ions interact much more frequently with the abundant neutrals through charge exchange. In particular close to the shock, where we observe the onset of the Kelvin-Helmholtz instability, collisions are still dominant and thus

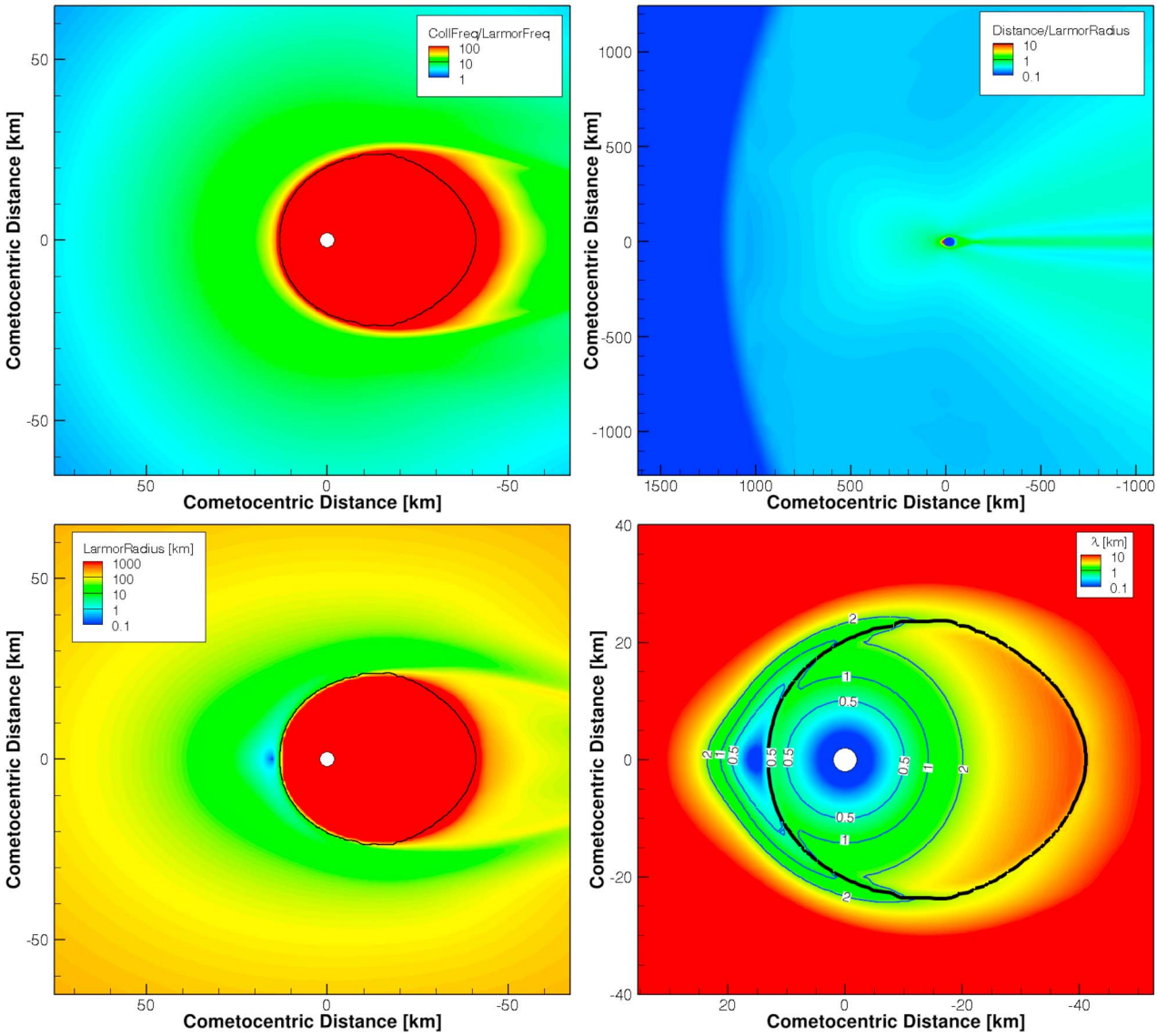

Figure 5. Applicability of the magnetohydrodynamics (MHD) model. (top left) The ratio of the ion-neutral collision frequency to the gyro frequency. The lower left plate shows the local ion gyroradius (if collisions were neglected) on the same scale. (top right) An overview of the ratio of the distance from the comet to the ion gyroradius and (bottom right) a close-up of the ion-neutral collisional mean free path as implemented through the ion-neutral friction term discussed in equation (2) including the 0.5, 1.0, and 2.0 km contour lines in blue color. The black contour lines denote the location of the inner shock where the plasma bulk velocity transitions from supersonic to subsonic speeds.

support the MHD description of the problem. The lower left plate shows the local ion gyroradius if the ions were able to gyrate freely. The top right plate shows the distance from the comet divided by the Larmor radius. This basically shows the ratio of the cometary structures in relation to the ion gyroradius. Once the ions and neutrals are collisionally decoupled and the modeled structures become smaller than the ion gyroradii it is expected that the real picture deviates from the MHD description. For higher production rate comets (e.g., 1P/Halley [see *Rubin et al.*, 2009]) where the bow shock is several hundreds of thousands of kilometers away and therefore its characteristic size larger than the ion gyroradius the MHD description might again be more adequate. Thus the formation of a bow shock as shown in our model at roughly 1200 km upstream of the comet is not questioned since the solar wind transitions from supersonic to subsonic speeds. However, its shape, location, and width might be affected by the kinetic behavior of the ions as demonstrated by *Delamere* [2006] in the case of comet 19P/Borrelly using a kinetic hybrid model. The upstream mass loading of the plasma streamlines is most likely altered while the cometary near field remains mostly unaffected. The plate on the lower right shows the collisional mean free path (or mean free path with respect to charge exchange) as implemented in our model through the ion-neutral friction parameter in equation (2) and includes the 0.5, 1.0, and 2.0 km mean free path

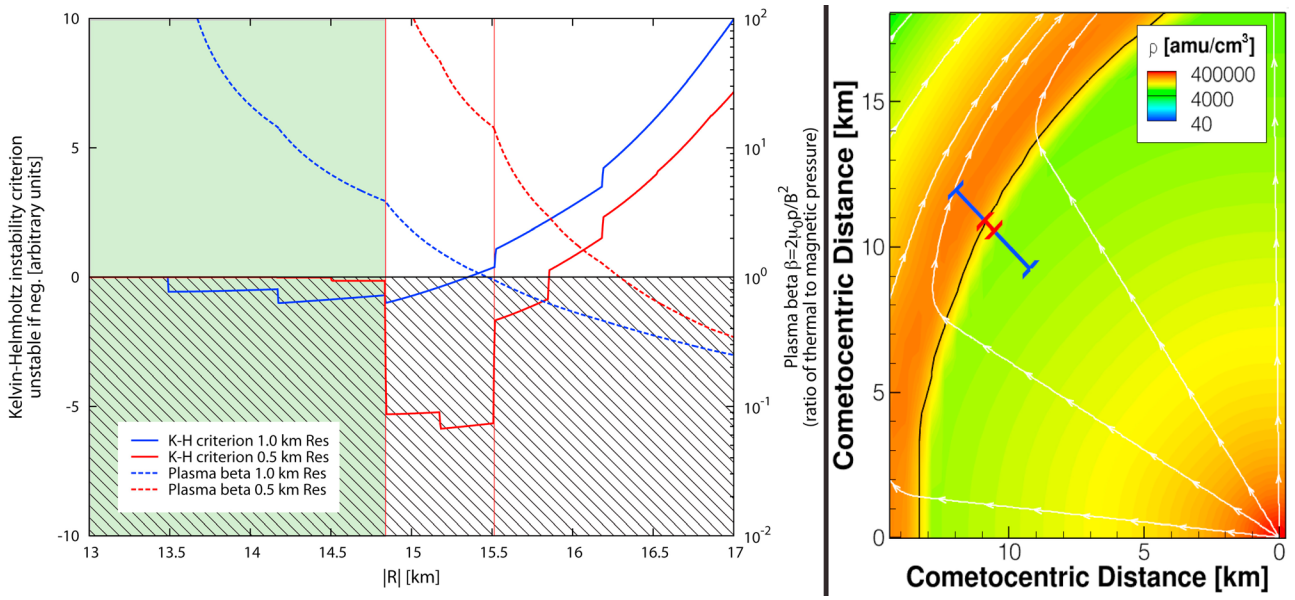

Figure 6. (left) Plotted is the right hand side of equation (11), extracted along a line from 13 km to 17 km distance from the comet in a 45 degrees angle for 1 km and 500 m cell resolutions, respectively. For negative values the plasma can become Kelvin-Helmholtz unstable (black hatched area). The green area denotes the region where the plasma dynamics are governed by the outflowing neutral gas through abundant ion-neutral collisions. The dashed lines are the corresponding plasma betas in the same locations in logarithmic scale (see second y axis). (right) The corresponding range from 13 to 17 km (blue) and the area where the system is most unstable in red, according to the thin vertical red lines in the left panel. Plotted are the mass density in amu/cm^3 and plasma streamlines similar to Figure 4 (top), the comet is located at (0,0) and the Sun is on the left hand side. The black contour line denotes the location of the inner shock where the plasma bulk velocity transitions from supersonic to subsonic speeds.

contour lines in blue. In three of the plates we added a black contour line showing the location of the inner shock where the plasma bulk velocity transitions from supersonic to subsonic speeds.

[22] As mentioned before, MHD shocks tend to be of a thickness between two to three cell sizes. Our simulations were therefore performed so that the resulting inner shock width was of the order of the local mean free path or larger. However the thickness of the real physical shock remains poorly constrained with this kind of model and the reader should therefore be cautioned and understand the presented results under those restrictions. In addition, as we will show later on, a dayside jet can also lead to Kelvin-Helmholtz instabilities – without any changes in the model's resolution.

[23] Figure 6 shows the right hand side of equation (11) as a function of cometocentric distance along a line 45 degrees off the Sun-comet axis in the y = 0 plane for two different cell sizes of 1 km and 500 m, respectively. For negative values the magnetic field is too weak to stabilize the Kelvin-Helmholtz wave formation (black hatched area). Indicated in green is the area where the plasma flow is governed by the collisional interaction with the neutrals through charge exchange processes. Outside this area the system becomes unstable in case of the smaller cell size in our simulations. While the plotted condition also indicates an unstable plasma flow for the coarser mesh, this case is still dominated by the neutral radially outflowing gas for most of this region and right outside numerical diffusion prevents the formation of the Kelvin-Helmholtz instability by limiting the Reynolds numbers in the flow [see *Frank et al.*, 1996; *Keppens et al.*, 1999]. It should be noted that the situation here is more complicated than considered in the classical Kelvin-Helmholtz instability criterion given in equations (10) and (11) due to the compressibility of the plasma. Therefore as discussed in equation (11) we also plotted the plasma beta obtained for both resolutions. Focusing to the region where the plasma becomes unstable according to the instability criterion (between the thin vertical red lines in Figure 6 at the inner shock) the thermal pressure exceeds the magnetic pressure by more than an order of magnitude in the unstable case (red dashed line) and thus equation (11) should be applicable. In the stable case (blue dashed), however, the plasma beta reaches unity on the outer edge and the reader should be cautioned that the results might differ from a more rigorous discussion as done by *Pu and Kivelson* [1983] for compressible plasmas. However, aside from the numerical diffusion that is different for both resolutions, there are also further, physical, complications due to the presence of the curved magnetic cavity boundary: the normal component of the flow is compressed in the shock and outside the plasma streamlines are bent tailward. Also the stabilization of the Kelvin-Helmholtz instability depends strongly on the strength and topology of the magnetic field that is draped around the magnetic cavity and aligned predominantly perpendicular to the plane shown in the right plate. Nevertheless, the condition from equation (11) applied here does reproduce both the required cell resolution and location of the onset of the Kelvin-Helmholtz instability in our MHD model. The

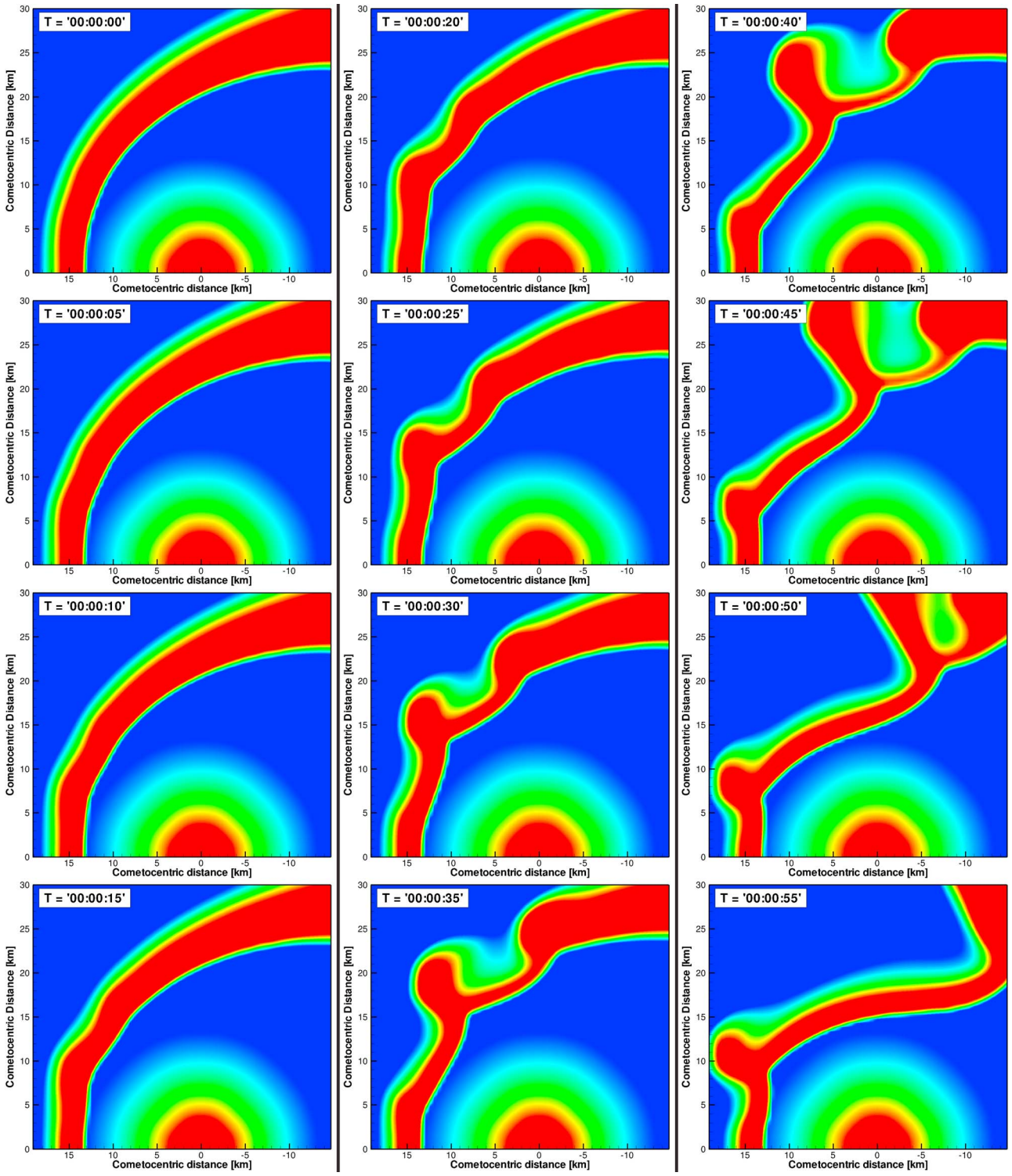

Figure 7. Modeled Kelvin-Helmholtz instability, triggered through increase of the cell resolution from 1 km to 500 m. The Sun is on the left hand side and the comet is located at the origin. The three columns top to bottom are 5-second intervals of plasma density cuts (arbitrary units) in the plane perpendicular to the magnetic field. Movie S1 can be found in the auxiliary material.[1]

plate on the right shows the location of the extracted lines with respect to the comet and the shock. The blue line shows the range plotted in the left plate from 13 to 17 km from the comet and the red line corresponds to the thin vertical red

[1]Auxiliary materials are available in the HTML. doi:10.1029/2011JA017300.

Table 2. Stable Versus Unstable Solutions[a]

	Uniform (f = 0)		Asymmetric (1 km res)			Asymmetric (f = 1)		
r_H (AU)	1 km res	500 m res	f = 0.05	f = 0.10	f = 0.15	1 km res	2 km res	4 km res
1.3	✓	✓	✓	✓	×	×		
2.0	✓	×	✓	×	×	×		
2.7	✓	×	✓	×	×	×	×	✓
3.0	✓	×	✓	×	×	×		
3.3	✓	×	✓	×	×	×		

[a]Collection of the model results showing whether a steady-state solution could be obtained (✓) or not (×). We investigated the influence of different cell resolutions (1 km and 0.5 km) on the simulations with uniform gas production rates (f = 0). Most jet cases (f > 0) were run with 1 km resolution, except for the f = 1 cases at 2.7 AU where we also ran cell sizes of 2 and 4 km. The total production rate of the individual runs are $1.5 \cdot 10^{27} \cdot (1+f)\ s^{-1}$ (equation (6)).

lines from the left panel for comparison. We have extracted these numbers also in various other angles across the shock and found similar results. Figure 6 also shows that the unstable Kelvin-Helmholtz layer is located at the inner shock where the plasma bulk speed transitions from supersonic to subsonic speeds.

[24] A more detailed investigation of the Kelvin-Helmholtz instability from a model run at 2.7 AU is shown in Figure 7. The figure shows 3 columns of snapshots in 5 second intervals top to bottom during the onset of the instability. We again plotted the plasma mass density but this time in arbitrary units to better illustrate the effect. The plasma shear flow just outside the magnetic cavity boundary is responsible for the typical Kelvin-Helmholtz wave formation. In these figures we investigate the plane perpendicular to the magnetic field as the components of the magnetic field times the wave vector $\vec{\mathbf{k}}$ in equation (10) are minimal in this direction and the onset of the Kelvin-Helmholtz instability can be observed easily.

[25] As mentioned above, the plasma shear flow just outside the magnetic cavity boundary is responsible for the onset of the instability when the condition of equation (10) is fulfilled. The wave growth is clearly visible from just a few seconds into the simulation and the individual plasma wave packets can be followed tailward around the magnetic cavity. As will be shown later, these packets are not limited to this plane but reach all around the magnetic cavity in filament-like structures. *Miura and Pritchett* [1982] applied an MHD approach to investigate the wave vector dependent growth rates of the Kelvin-Helmholtz instability for compressible plasmas. Their results, applied to the parameter range applicable here, indicate maximum growth rates for wavelengths close to 8 times the shear layer thickness. Figure 6 indicates a shear layer thickness on the order of 1 km, which is in line with the approximately 8 km wave length found in Figure 7 (see, e.g., 15 seconds into the simulation, measured at the contact surface) in the plane perpendicular to the magnetic field. Clearly, this is only a first order approach and further complication is expected from the complex shape of the cavity with varying conditions along its boundary as well as the draped magnetic field lines.

[26] Table 2 presents a collection of the obtained results. The first column lists the heliocentric distance and columns two and three show whether a steady state solution could be obtained using a cell resolution of 500 m or 1 km, respectively. A uniform neutral gas production rate (f = 0) of $1.5 \cdot 10^{27}\ s^{-1}$ was used. It can be seen that the increased magnetic field closer to the Sun can stabilize the formation of Kelvin-Helmholtz waves for the case of 500 m cell resolution. Consequently, the Kelvin-Helmholtz instability could also be initiated through a transition of the upstream magnetic field values from the 1.3 to 2.0 AU (Table 1) without changing the resolution. This, however, is computationally more expensive than the here shown initiation through a resolution change.

3.2. Asymmetric Neutral Gas Production

[27] Table 2 also shows the various model runs investigating different asymmetric neutral gas productions. Columns 4 to 6 show whether a steady state result could be obtained ($T_{sim} = \infty$ in equation (7)). The asymmetric gas production was varied from 5% to 15% (f = 0.05 to 0.15) of the symmetric gas production rate. In columns 7 to 9 we also investigated the influence of the mesh resolution at the shock on the stability of the numerical solution for the case of 2.7 AU with an asymmetric production equal to the symmetric component (f = 1). As discussed above, in MHD the thickness of the shock is on the order of two to three cell sizes and therefore affects the resulting shear flow. Thus by decreasing the resolution to 4 km (MHD shock width 8 km – 12 km) the magnetic cavity boundary can become stable again.

[28] For the following case study, starting from a stable magnetic cavity, we investigate the effect of an increasing, time-dependent, asymmetric neutral gas production rate. We assume the same symmetric component of the neutral gas production rate ($Q_{sym} = 1.5 \cdot 10^{27}\ s^{-1}$) and subsequently increase the asymmetric part. The right hand side of Figure 4 (right) shows the same quantities as on the left hand side but for an asymmetric gas production rate. The Sun is again on the left hand side and the magnetic field is almost symmetrically draped around the cavity as can be seen in the bottom plate. The upper plate shows the plasma mass density and the plasma streamlines in particular also across the shock. Plotted again is the plane containing the magnetic field. The sunward directed component of the neutral gas distribution is clearly influencing the shape of the magnetic cavity. The plasma streamlines are now directed in the upstream direction according to the coplanarity relation in equation (9). Following the single fluid MHD equations in equation (1) the ions are tied to the magnetic field and thus the magnetic field lines are filled from both sides and increasingly mass loaded on the sunward side of the cavity. The only way for the plasma to escape is the through the plane perpendicular to the magnetic field. Figure 8 shows the distribution of plasma in the plane perpendicular to the solar wind flow direction. In the case of the asymmetric neutral gas distribution adopted here, this leads to two distinct enhancements

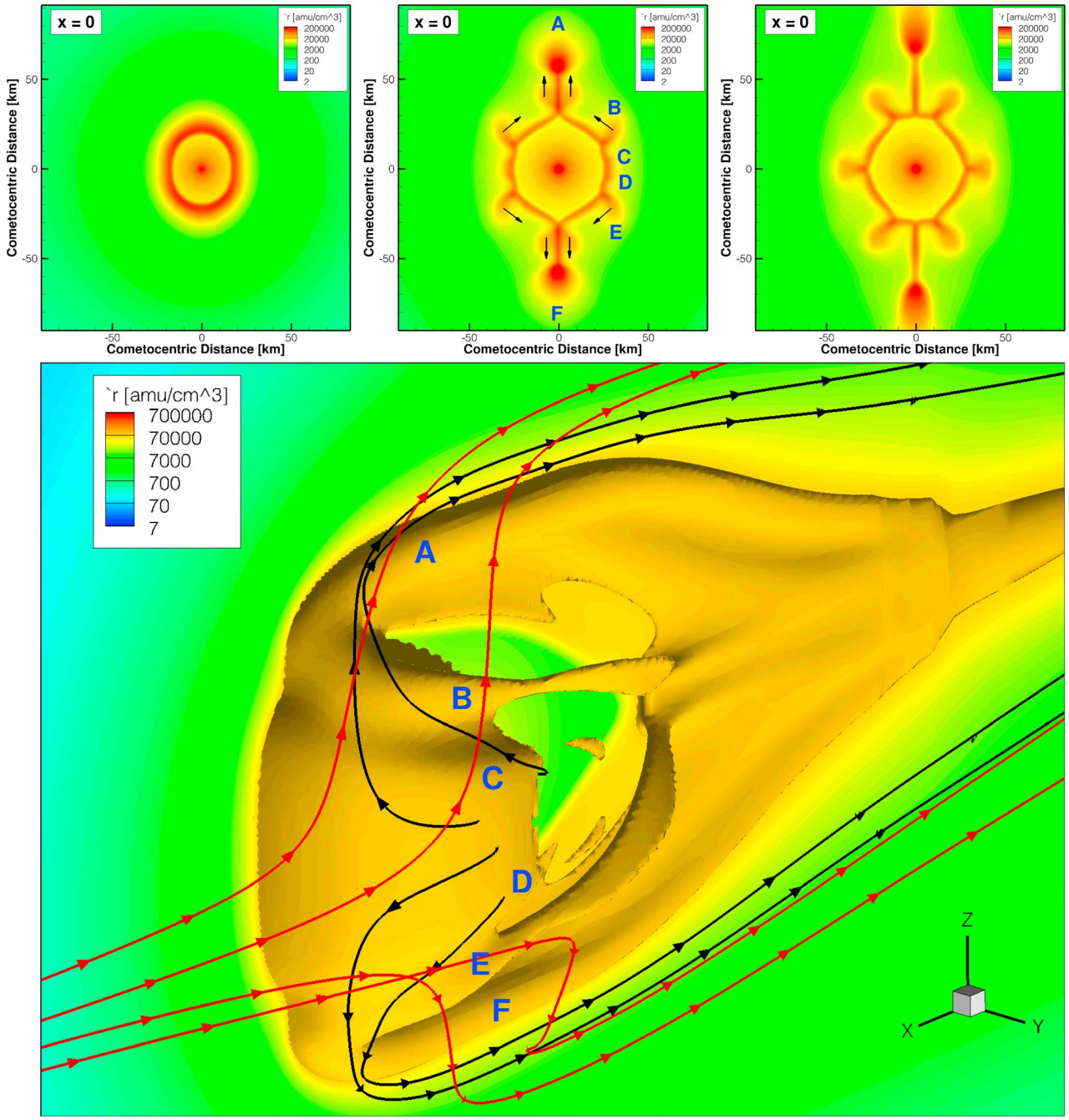

Figure 8. Plasma density in the plane perpendicular to the upstream solar wind direction with the comet in the center. The magnetic field is aligned horizontally. (top left) Spherically symmetric production rate with tailward bending of the plasma streamlines around the whole cavity which leads to a uniform tailward flowing plasma. The two plates on the top right show the case of a dayside directed asymmetric neutral gas distribution at two distinct times. Plasma streamlines are bent sunward and the tailward flow is enhanced in the plane perpendicular to the magnetic field creating flux tubes in both magnetic north and south (see also Figure 4). The small filaments on the outside of the cavity coincide with the waves shown in Figure 7 and the blue letters (B-E) in thebottom plate. They move toward either the northern or the southern flux tubes and temporarily push these further out. In stable jet cases these filaments vanish but the flux tubes remain (A and F). The bottom plate shows a 3D density iso-surface with a cut in the y = 0 plane for the jet case. Plasma streamlines originating from the comet (black) and upstream (red) are forced around the comet in the plane perpendicular to the magnetic field.

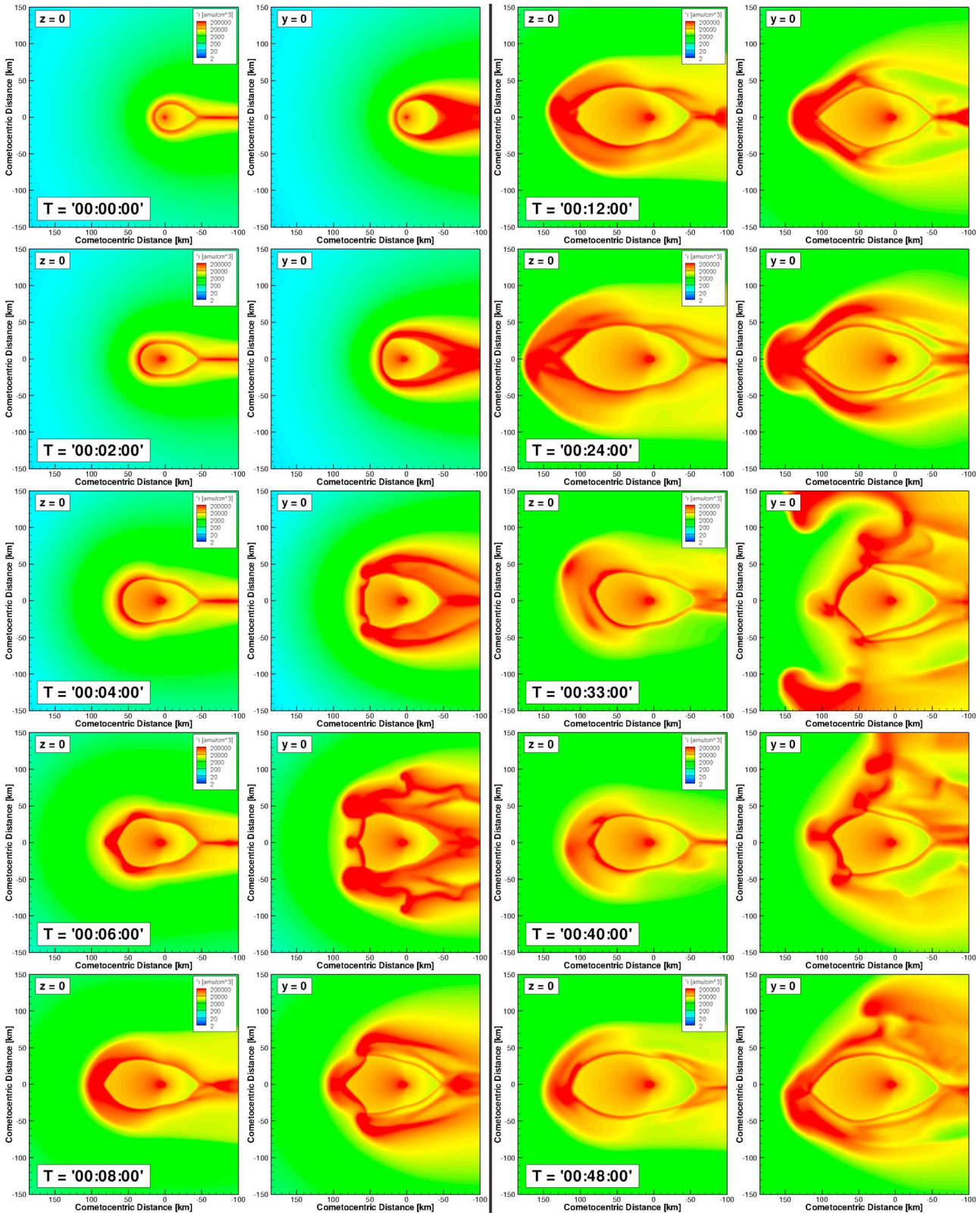

Figure 9. Two columns of top to bottom time-dependent z = 0 (containing the magnetic field) and y = 0 plane cuts for 1 hour of real time showing the plasma mass density. The asymmetric neutral gas production is increased from zero to the same value of the symmetric gas production rate over a time span of 3 min thus in effect doubling the total production rate. The Sun is on the left hand side and the comet is located at (0, 0). Movie S2 can be found in the auxiliary material.

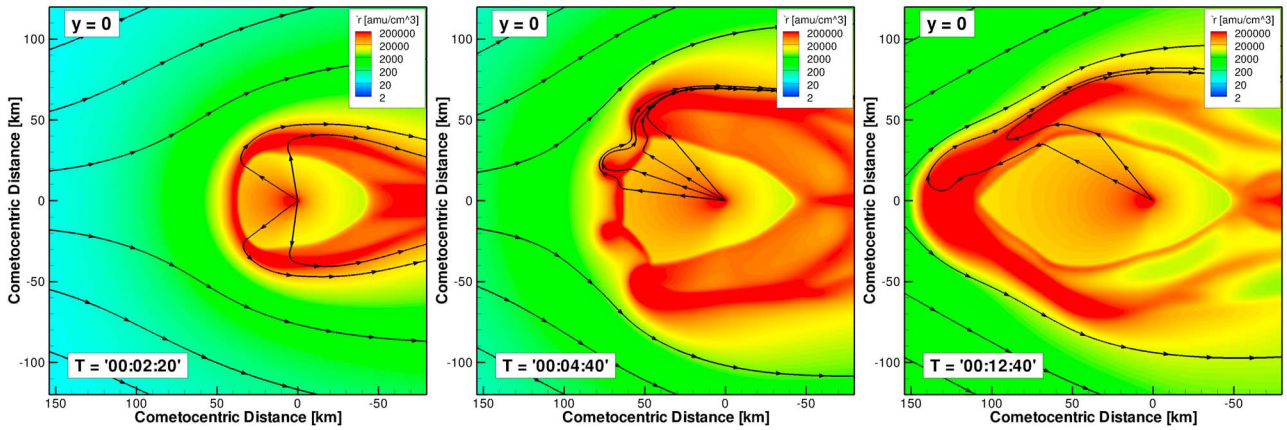

Figure 10. Three cuts at different times through the plane perpendicular to the magnetic field (y = 0) showing the plasma mass density and several streamlines (see also Figure 9).

in plasma density north and south of the cavity (denoted by A and F).

[29] In the following we will show that the results using the asymmetric neutral gas distribution from Figures 4 and 8 can again turn unstable depending on the chosen boundary conditions. In particular it can be seen that in specific locations on the upstream side the shear flows in the plasma are increased because of the plasma streamlines that are bent forward at the shock. This increase in shear flow in turn is then again responsible for the formation of the Kelvin-Helmholtz instability which reaches around the whole cavity as denoted by the letters B – E in Figure 8.

[30] In Figure 9 we show a time series of the plasma mass density. For this specific simulation we started with a spherically symmetric neutral gas distribution of $1.5 \cdot 10^{27}$ s^{-1} and increased a sunward directed asymmetric component (equation (4)) over the time-span of three minutes from f = 0 to f = 1 thus in effect doubling the total neutral gas production rate (equation (6)). The times adapted in this case are random but chosen so that the change in neutral gas distribution is rather smooth in comparison to the time of the plasma propagation from the nucleus to the upstream cavity boundary (we use a neutral gas outflow velocity of 1 km/s as given in Table 1). Here the resolution of the computational mesh at the inner shock was kept constant. We limit the results shown to a total real-time duration of 1 hour and therefore neglect the comet's rotation. We also keep the upstream solar wind conditions and solar photo rates constant as listed in Table 1. Therefore the results presented here do not require a sustained production of this strength; an outburst in the timescale of one hour can be enough for the occurrence of the phenomena discussed here. We will discuss further limitations of this simple model in section 4. Plotted is a series of y = 0 and z = 0 plane snapshots at the indicated times. The plane with z = 0 contains the undisturbed interplanetary magnetic field. Several phases can be identified with the onset of this dayside dominated neutral gas production rate:

[31] 1. The distance of the cometary cavity boundary is increased on the dayside, the shape on the subsolar side is still blunt and thus all the plasma streamlines remain bent backwards ($T_{sim} < \sim 2$ min).

[32] 2. Later the cavity becomes elongated on the sides and the plasma streamlines bend sunward and the resulting increase in shear flow can lead to Kelvin-Helmholtz instabilities.

[33] 3. Sunward bent streamlines force the plasma around the comet mostly in the plane perpendicular to the magnetic field (y = 0 plane).

[34] 4. While there are some disturbances in the plane containing the magnetic field (z = 0 plane), the perpendicular plane containing the tailward flowing plasma is much more affected (see, e.g., T_{sim} = 6 min).

[35] 5. Once the shape of the underlying neutral gas is forced upon the plasma distribution the shear flow is increased as the plasma streamlines are bent towards the Sun on most of the sunward side of the magnetic cavity (see, e.g., $T_{sim} > 8$ min).

[36] 6. Our model also suggests that a distinct pattern in the plasma density can form where the forward flow is separated from the tailward flow (see T_{sim} = 24 min). In the y = 0 plane two enhancements in plasma density can be observed. Apart from the inner shock the tailward flowing plasma leads to a stream of enhanced plasma density. We will discuss this further below.

[37] 7. Because we are using a Parker spiral for the upstream interplanetary magnetic field the symmetry is broken. This becomes obvious also in the y = 0 plane for $T_{sim} > 24$ min when the plasma outflow in +y direction differs from the -y direction. Plasma wave packets are released at different times from both sides despite the symmetric distribution of the neutral jet in this simulation.

[38] For more details we plotted three of the y = 0 snapshots together with plasma streamlines. Figure 10 (left) shows the state of the simulation 02:20 minutes after the onset of the jet but before developing Kelvin-Helmholtz instabilities. This is also a typical result for the stable solutions listed in Table 2: the plasma streamlines are still bent backwards and the shape of the cavity boundary resembles a rather blunt tear drop. The middle plate shows the result 04:40 minutes into the simulation after Kelvin-Helmholtz instabilities have developed. Here, based on the shape of the magnetic cavity boundary plasma wave packets are formed where the bending of streamlines flips orientation at the

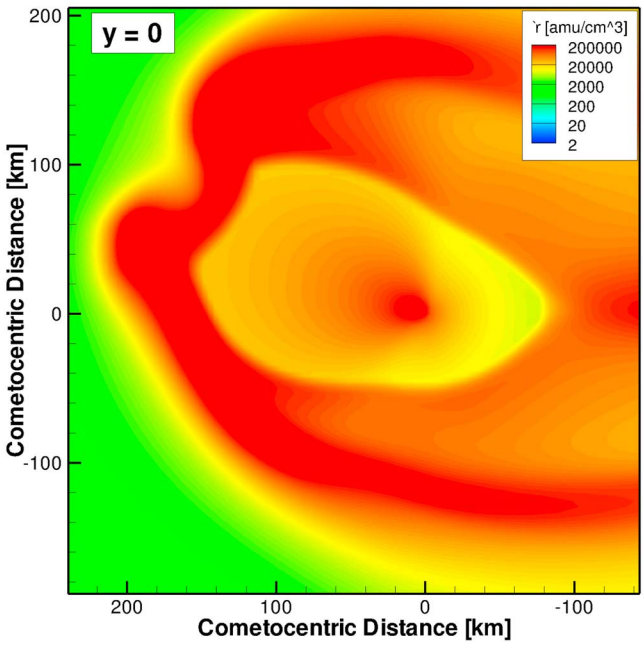

Figure 11. Example of the plasma mass density with the Sun on the left hand side and the comet centered at the origin. The asymmetric neutral gas production is aligned 20 degrees off axis from the sub-solar direction and the mean ion mass has been increased to mimic a CO/CO_2 dominated comet.

shock. These plasma wave packets are continuously filled from both sides as they are pushed tailward around the cavity boundary (this is also responsible for the filament-like and time-dependent structures denoted by B – E in Figure 8). The plate on the right side shows a snapshot 12:40 minutes into the simulation where the neutral profile is already imposed upon the distribution of the plasma by the ion-neutral friction force. Apart from the shock a distinct tailward flow of the plasma can be observed. All the plasma that is inside the cavity on the sunward side of the comet (positive horizontal coordinate in this figure) is forced tailward in this particular plane because in the perpendicular plane the ions are tied to the magnetic field lines and pushed to the subsolar point of the cavity as discussed previously and shown in Figure 4. Accordingly, in single fluid MHD, also the upstream plasma streamlines are forced into either the north or south tailward plasma flux tubes.

[39] For the sake of completeness we also investigated the case of an asymmetric neutral gas distribution peaked offline from the Sun-comet line by adjusting $\vec{\mathbf{x}}$ in equation (5). Figure 11 shows the corresponding plasma mass density at a random point in time for a CO/CO_2 dominated jet. The results show that breaking the jet symmetry with respect to the solar wind flow direction can still lead to the formation of Kelvin-Helmholtz instabilities but the disturbed plasma outflow can be observed predominantly in the direction of the tilt (upward in the geometry of Figure 11). Also the choice of the dominating cometary specie (H_2O vs CO/CO_2) does not change the overall phenomena but can influence the onset of the discussed features. The choice of mean ion mass directly influences the mass loading, the different ion-neutral collisional cross sections (neglected here) affects the ion-neutral friction, and the different ion-electron recombination rates can move the location of the magnetic cavity boundary as well.

4. Limitations

[40] The model is based on a number of assumptions. The assumed neutral model is only a crude approximation of the expected distribution, dynamics, and composition. There are various studies discussing expected neutral environments at comet 67P/Churyumov-Gerasimenko as Rosetta follows the comet from almost 3.5 AU all the way to and past perihelion [e.g., *Crifo et al.*, 2003]. *Combi* [1996] and *Tenishev et al.* [2008] discuss results from a coupled nucleus - coma model whereas *Tenishev et al.* [2011] further include the close-tied neutral dust environment. These works show a much more complex neutral environment with additional non-radial velocity components. Also collisions between the parent species as well as the dissociated products can influence neutral speeds and abundances. The gas production rates used for 2.7 AU are close to the modeled values given by *De Sanctis et al.* [2010]. They might be higher closer to the Sun and certainly lower farther away. We also have shown that jets of rather short timescales of less than one hour can already lead to the modeled instabilities. This could be for instance an active patch on the surface, a jet, or just a dayside dominated production rate. For much longer timescales the comet's rotation influences the presented results and needs to be taken into account. Accordingly, but not explicitly shown here, a short-time change in the upstream solar wind conditions such as a decrease in the magnetic field strength could yield similar results.

[41] For the sake of simplicity we also kept the upstream interplanetary magnetic field as well as the solar wind speed and direction constant for any given heliocentric distance. The results shown herein thus only present a small fraction of the conditions expected for the comet on its orbit, but do illustrate the range of phenomena that would be associated with a cometary Kelvin-Helmholtz instability.

[42] Several limitations come from the fluid character in the magnetohydrodynamics approach. The model is most suitable for highly collisional plasmas and length scales larger than the ion gyroradius. Furthermore a small (or no) resistivity is required for the applicability of our model. Generally the near comet region is very much collision dominated for the production rates used in the presented runs. It is also this charge exchange between the neutral gas with the accumulated plasma that counteracts the magnetic pressure gradient force and the magnetic curvature force and thus forms the magnetic cavity that is the basis of this work. Further away from the comet the neutral gas density drops with $\sim 1/r^2$ and the mean free path increases. In Figure 5 we have plotted the ratio of the collision frequency to the ion gyro frequency. In the region of the magnetic cavity boundary where we observe the onset of the instability caused by the plasma shear flow, the collision frequency is more than one order of magnitude higher than the corresponding ion gyro frequency. Even though for some of the cases the formation of a bow shock as predicted by the MHD model results is questionable, the close region around the inner

shock should be much better captured by our model despite the fact that MHD cannot resolve the individual ion's gyro motion. Nevertheless the fluid description of the plasma remains a limiting factor in the presented results.

[43] Based on the numerical diffusion of the applied scheme and the computational resolution around the magnetic cavity, the onset of the instability varies. Therefore it remains difficult to pinpoint the exact boundary conditions for which the instability occurs. In particular the link between the numerical and the real physical diffusion of the problem at hand is hard to establish and well beyond the scope of this work. Our results depend on the actual physics at the inner shock which cannot be self consistently modeled in MHD.

[44] As described before, our model assumes one single type of ions, namely cometary heavy ions. While this is certainly only a crude approximation for the free streaming solar wind the major characteristics close to the nucleus should be well captured (as shown for comet 1P/Halley by *Rubin et al.* [2009]). The presented results should therefore be adopted with caution and under these outlined restrictions.

[45] The phenomena discussed here in this paper have not been observed in the past. The Giotto spacecraft crossed the magnetic cavity boundary of comet 1P/Halley behind the terminator during the inbound leg of the fly-by. In this location it is difficult to distinguish between these cases because also our MHD model predicts tailward bent streamlines in line with the Ion Mass Spectrometer observations [*Altwegg et al.*, 1993; *Rubin et al.*, 2009]. Unfortunately the IMS did not survive the fly-by to obtain measurements on the outbound path. Furthermore our model also predicts rather stable magnetic cavities due to the larger magnetic field for small heliocentric distances such as the Giotto flyby at 0.9 AU. As discussed before, the phenomena depends on the distribution of the neutral gas and is concentrated in the plane perpendicular to the upstream magnetic field. Given a fly-by just a few degrees out of this plane and the effects presented here might not be observable or at least greatly subdued.

[46] For the upcoming Rosetta mission the measurement of the thermal cold plasma itself is going to be a daunting task. For instance, a combination of measurements performed by the magnetometer (MAG), the Ion Electron Sensor (IES), the Ion Composition Analyzer (ICA), the Langmuir Probe (LAP), and the Mutual Impedance Probe (MIP) of the Rosetta Plasma Consortium (RPC) [see *Carr et al.*, 2007] as well as the Double Focusing Mass Spectrometer (DFMS) and the Reflectron-type Time of Flight mass spectrometer (RTOF) of the Rosetta Orbiter Spectrometer for Ion and Neutral Analysis (ROSINA) [see *Balsiger et al.*, 2007] are all capable to observe such phenomena – if they exist. *Berthelier and Roussel* [2004] and *Roussel and Berthelier* [2004] have shown that measuring low energy thermal plasma can be significantly compromised by spacecraft charging processes. The ROSINA RTOF and DFMS for instance require special attraction grids to penetrate the sheath around the spacecraft to measure the low energy thermal ions [*Rubin et al.*, 2006]. Nevertheless, there are more instruments, including the lander, that can provide further important clues on these effects.

[47] Even if the magnetic cavity remains stable an enhanced tailward flow of plasma in the plane perpendicular to the magnetic field and the associated sunward bent streamlines might be observable. The optimal location for the observations of the phenomena discussed here is right outside the inner shock with the field-of-view of the named instruments pointed in both the direction of the comet and also the undisturbed solar wind flow. Obviously the latter geometry is not very interesting for most remote sensing instruments aboard Rosetta such as the cameras and might even interfere with spacecraft attitude and safety requirements. However the magnetometer instrument could still prove very useful in detecting not only the boundary of the magnetic field free zone but also the instabilities propagating tailward in the plane perpendicular to the undisturbed upstream magnetic field, which leave their signatures in the components of the magnetic field.

5. Summary and Conclusions

[48] Our MHD model suggests different plasma flow patterns around the comet depending on the distribution of the neutral gas in the coma and the upstream boundary conditions. We investigated asymmetric sunward oriented jets that alter the flow of the plasma around the magnetic cavity, the innermost magnetic field-free zone around the comet. Plasma streamlines can flip orientation at this shock and bend forward before again being pushed back around the cavity in the plane perpendicular to the magnetic field. The resulting increase in shear flow might even lead to Kelvin-Helmholtz instabilities, leaving very distinct patterns predominantly in the plane perpendicular to the magnetic field. We also obtained similar results when such a jet or a patch on the surface of the comet becoming active was initiated in a time-dependent manner and propagates through the coma at the neutral gas' velocity. Given the limitations of the MHD approach, we cannot provide exact predictions about the onset of these effects, and so the results presented herein remain somewhat qualitative. However, on the Rosetta spacecraft the Rosetta Plasma Consortium package as well as the Rosetta Orbiter Spectrometer for Ion and Neutral Analysis are both able to investigate the local plasma properties and find traces of the phenomena discussed here.

[49] **Acknowledgments.** This work has been supported by JPL subcontract 1266313 under NASA grant NMO710889, NASA Planetary Atmospheres program grant NNX09AB59G, and grant AST-0707283 from the NSF Planetary Astronomy program. We thank the comet modeling team from the International Space Science Institute (ISSI) for the fruitful discussions.

[50] Masaki Fujimoto thanks the reviewers for their assistance in evaluating this paper.

References

Altwegg, K., H. Balsiger, J. Geiss, R. Goldstein, W.-H. Ip, A. Meier, M. Neugebauer, H. Rosenbauer, and E. Shelley (1993), The ion population between 1300 km and 230,000 km in the coma of comet P/Halley, *Astron. Astrophys.*, *279*, 260–266.

Balsiger, H., et al. (1986), Ion composition and dynamics at comet Halley, *Nature*, *321*, 330–334.

Balsiger, H., et al. (2007), Rosina Rosetta Orbiter Spectrometer for Ion and Neutral Analysis, *Space Sci. Rev.*, *128*, 745–801, doi:10.1007/s11214-006-8335-3.

Benna, M., and P. R. Mahaffy (2006), New multi-fluid MHD model of comet 26P/Grigg-Skjellerup: Extrapolation to comet 67P/Churyumov-Gerasimenko, *Geophys. Res. Lett.*, *33*, L10103, doi:10.1029/2006GL026197.

Benna, M., and P. Mahaffy (2007), Multi-fluid model of comet 1P/Halley, *Planet. Space Sci.*, *55*, 1031–1043, doi:10.1016/j.pss.2006.11.019.

Berthelier, J., and J. Roussel (2004), A study of the electrical charging of the Rosetta orbiter: 2. Experimental tests in a laboratory plasma, *J. Geophys. Res.*, *109*, A01105, doi:10.1029/2003JA009834.

Boardsen, S. A., T. Sundberg, J. A. Slavin, B. J. Anderson, H. Korth, S. C. Solomon, and L. G. Blomberg (2010), Observations of Kelvin-Helmholtz waves along the dusk-side boundary of Mercury's magnetosphere during MESSENGER's third flyby, *Geophys. Res. Lett.*, *37*, L12101, doi:10.1029/2010GL043606.

Carr, C., et al. (2007), RPC: The Rosetta Plasma Consortium, *Space Sci. Rev.*, *128*, 629–647, doi:10.1007/s11214-006-9136-4.

Chandrasekhar, S. (1961), *Hydrodynamic and Hydromagnetic Stability*, Clarendon, Oxford, U. K.

Chen, D.-H., and L.-Z. Liu (1992), Stability of the cometary ionopause, *Astrophys. Space Sci.*, *189*, 45–55.

Combi, M. R. (1996), Time-dependent gas kinetics in tenuous planetary atmospheres: The cometary coma, *Icarus*, *123*, 207–226, doi:10.1006/icar.1996.0150.

Cravens, T. E. (1987), Ion energetics in the inner coma of Comet Halley, *Geophys. Res. Lett.*, *14*, 983–986, doi:10.1029/GL014i010p00983.

Cravens, T. E. (1989a), Cometary plasma boundaries, *Adv. Space Res.*, *9*, 293–304, doi:10.1016/0273-1177(89)90452-3.

Cravens, T. E. (1989b), The solar wind interaction with non-magnetic bodies and the role of small-scale structures, in *Solar System Plasma Physics*, *Geophys. Monogr. Ser.*, vol. 54, edited by J. H. Waite Jr., J. L. Burch, and R. L. Moore, pp. 353–366, AGU, Washington, D. C., doi:10.1029/GM054p0353.

Crifo, J. F., G. A. Loukianov, A. V. Rodionov, and V. V. Zakharov (2003), Navier-Stokes and direct Monte Carlo simulations of the circumnuclear coma II. Homogeneous, aspherical sources, *Icarus*, *163*, 479–503, doi:10.1016/S0019-1035(03)00041-1.

De Sanctis, M. C., J. Lasue, M. T. Capria, G. Magni, D. Turrini, and A. Coradini (2010), Shape and obliquity effects on the thermal evolution of the Rosetta target 67P/Churyumov-Gerasimenko cometary nucleus, *Icarus*, *207*, 341–358, doi:10.1016/j.icarus.2009.11.009.

Delamere, P. A. (2006), Hybrid code simulations of the solar wind interaction with Comet 19P/Borrelly, *J. Geophys. Res.*, *111*, A12217, doi:10.1029/2006JA011859.

Delamere, P. A. (2009), Hybrid code simulations of the solar wind interaction with Pluto, *J. Geophys. Res.*, *114*, A03220, doi:10.1029/2008JA013756.

Delamere, P. A., R. J. Wilson, and A. Masters (2011), Kelvin-Helmholtz instability at Saturn's magnetopause: Hybrid simulations, *J. Geophys. Res.*, *116*, A10222, doi:10.1029/2011JA016724.

Draine, B. T., and C. F. McKee (1993), Theory of interstellar shocks, *Annu. Rev. Astron. Astrophys.*, *31*, 373–432, doi:10.1146/annurev.aa.31.090193.002105.

Eberhardt, P., and D. Krankowsky (1995), The electron temperature in the inner coma of comet P/Halley, *Astron. Astrophys.*, *295*, 795–806.

Ershkovich, A. I. (1980), Kelvin-Helmholtz instability in type-1 comet tails and associated phenomena, *Space Sci. Rev.*, *25*, 3–34, doi:10.1007/BF00200796.

Ershkovich, A. I., D. Prialnik, and A. Eviatar (1986), Instability of a comet ionopause: Consequences of collisions and compressibility, *J. Geophys. Res.*, *91*, 8782–8788, doi:10.1029/JA091iA08p08782.

Eviatar, A., and B. E. Goldstein (1988), A unidimensional model of comet ionosphere structure, *J. Geophys. Res.*, *93*, 1759–1765, doi:10.1029/JA093iA03p01759.

Frank, A., T. W. Jones, D. Ryu, and J. B. Gaalaas (1996), The magnetohydrodynamic Kelvin-Helmholtz instability: A two-dimensional numerical study, *Astrophys. J.*, *460*, 777–, doi:10.1086/177009.

Goedbloed, J., R. Keppens, and S. Poedts (2010), *Advanced Magnetohydrodynamics: With Applications to Laboratory and Astrophysical Plasmas*, Cambridge Univ. Press, New York.

Gombosi, T. I. (2004), *Physics of the Space Environment*, Cambridge Univ. Press, Cambridge, U. K.

Gombosi, T. I., D. L. De Zeeuw, R. M. Häberli, and K. G. Powell (1996), Three-dimensional multiscale MHD model of cometary plasma environments, *J. Geophys. Res.*, *101*, 15,233–15,252, doi:10.1029/96JA01075.

Gortsas, N., U. Motschmann, E. Kührt, K. Glassmeier, K. C. Hansen, J. Müller, and A. Schmidt (2010), Global plasma-parameter simulation of Comet 67P/Churyumov-Gerasimenko approaching the Sun, *Astron. Astrophys.*, *520*, A92, doi:10.1051/0004-6361/201014761.

Hansen, K. C., T. Bagdonat, U. Motschmann, C. Alexander, M. R. Combi, T. E. Cravens, T. I. Gombosi, Y.-D. Jia, and I. P. Robertson (2007), The plasma environment of Comet 67P/Churyumov-Gerasimenko throughout the Rosetta main mission, *Space Sci. Rev.*, *128*, 133–166, doi:10.1007/s11214-006-9142-6.

Ip, W., and W. I. Axford (1987), The formation of a magnetic-field-free cavity at Comet Halley, *Nature*, *325*, 418–419, doi:10.1038/325418a0.

Jia, Y. D., M. R. Combi, K. C. Hansen, T. I. Gombosi, F. J. Crary, and D. T. Young (2008), A 3-D global MHD model for the effect of neutral jets during the Deep Space 1 Comet 19P/Borrelly flyby, *Icarus*, *196*, 249–257, doi:10.1016/j.icarus.2008.03.010.

Keppens, R., G. Tóth, R. H. J. Westermann, and J. P. Goedbloed (1999), Growth and saturation of the Kelvin-Helmholtz instability with parallel and antiparallel magnetic fields, *J. Plasma Phys.*, *61*, 1–19, doi:10.1017/S0022377898007223.

Kivelson, M. G., and Z.-Y. Pu (1984), The Kelvin-Helmholtz instability on the magnetopause, *Planet. Space Sci.*, *32*, 1335–1341, doi:10.1016/0032-0633(84)90077-1.

Linde, T. J. (1998), A three-dimensional adaptive multifluid MHD model of the heliosphere, PhD thesis, Univ. of Mich., Ann Harbor.

Masters, A., N. Achilleos, C. Bertucci, M. K. Dougherty, S. J. Kanani, C. S. Arridge, H. J. McAndrews, and A. J. Coates (2009), Surface waves on Saturn's dawn flank magnetopause driven by the Kelvin-Helmholtz instability, *Planet. Space Sci.*, *57*, 1769–1778, doi:10.1016/j.pss.2009.02.010.

Miura, A., and P. L. Pritchett (1982), Nonlocal stability analysis of the MHD Kelvin-Helmholtz instability in a compressible plasma, *J. Geophys. Res.*, *87*, 7431–7444, doi:10.1029/JA087iA09p07431.

Möstl, U. V., N. V. Erkaev, M. Zellinger, H. Lammer, H. Gröller, H. K. Biernat, and D. Korovinskiy (2011), The Kelvin-Helmholtz instability at Venus: What is the unstable boundary?, *Icarus*, *216*, 476–484, doi:10.1016/j.icarus.2011.09.012.

Motschmann, U., and E. Kührt (2006), Interaction of the solar wind with weak obstacles: Hybrid simulations for weakly active comets and for Mars, *Space Sci. Rev.*, *122*, 197–208, doi:10.1007/s11214-006-6218-2.

Neubauer, F. M., et al. (1986), First results from the Giotto magnetometer experiment at comet Halley, *Nature*, *321*, 352–355.

Ogilvie, K. W., and R. J. Fitzenreiter (1989), The Kelvin-Helmholtz instability at the magnetopause and inner boundary layer surface, *J. Geophys. Res.*, *94*, 15,113–15,123, doi:10.1029/JA094iA11p15113.

Powell, K. G., P. L. Roe, T. J. Linde, T. I. Gombosi, and D. L. de Zeeuw (1999), A solution-adaptive upwind scheme for ideal magnetohydrodynamics, *J. Comput. Phys.*, *154*, 284–309, doi:10.1006/jcph.1999.6299.

Pu, Z.-Y., and M. G. Kivelson (1983), Kelvin-Helmholtz instability at the magnetopause: Solution for compressible plasmas, *J. Geophys. Res.*, *88*, 841–861, doi:10.1029/JA088iA02p00841.

Pu, Z.-Y., and M. G. Kivelson (1984), Kelvin-Helmholtz instability and MHD surface waves on Saturn's magnetopause, *Chin. J. Space Sci.*, *4*, 105–111.

Roussel, J., and J. Berthelier (2004), A study of the electrical charging of the Rosetta orbiter: 1. Numerical model, *J. Geophys. Res.*, *109*, A01104, doi:10.1029/2003JA009836.

Rubin, M., K. Altwegg, A. Jäckel, and H. Balsiger (2006), Development of a low energy ion source for ROSINA ion mode calibration, *Rev. Sci. Instrum.*, *77*, 103302, doi:10.1063/1.2358708.

Rubin, M., K. C. Hansen, T. I. Gombosi, M. R. Combi, K. Altwegg, and H. Balsiger (2009), Ion composition and chemistry in the coma of Comet 1P/Halley: A comparison between Giotto's Ion Mass Spectrometer and our ion-chemical network, *Icarus*, *199*, 505–519, doi:10.1016/j.icarus.2008.10.009.

Sauer, K., and K. Baumgaertel (1986), Fluid simulation of Halley's ionosphere, in *ESLAB Symposium on the Exploration of Halley's Comet*, edited by B. Battrick, E. J. Rolfe, and R. Reinhard, *Eur. Space Agency Spec. Publ., ESA SP-250*, 401–404.

Schleicher, D. G., L. M. Woodney, and R. L. Millis (2003), Comet 19P/Borrelly at multiple apparitions: Seasonal variations in gas production and dust morphology, *Icarus*, *162*, 415–442, doi:10.1016/S0019-1035(02)00072-6.

Schmidt, H. U., R. Wegmann, and F. M. Neubauer (1986), MHD-model for Comet Halley, in *ESLAB Symposium on the Exploration of Halley's Comet*, edited by B. Battrick, E. J. Rolfe, and R. Reinhard, *Eur. Space Agency Spec. Publ.*, *ESA SP-250*, 43–46.

Tenishev, V., M. Combi, and B. Davidsson (2008), A global kinetic model for cometary comae: The evolution of the coma of the Rosetta target comet Churyumov-Gerasimenko throughout the mission, *Astrophys. J.*, *685*, 659–677, doi:10.1086/590376.

Tenishev, V., M. R. Combi, and M. Rubin (2011), Numerical simulation of dust in a cometary coma: Application to Comet 67P/Churyumov-Gerasimenko, *Astrophys. J.*, *732*, 104, doi:10.1088/0004–637X/732/2/104.

Tóth, G., et al. (2005), Space Weather Modeling Framework: A new tool for the space science community, *J. Geophys. Res.*, *110*, A12226, doi:10.1029/2005JA011126.

Wiehle, S., U. Motschmann, N. Gortsas, K.-H. Glassmeier, J. Müller, and C. Koenders (2011), Simulation of cometary jets in interaction with the solar wind, *Adv. Space Res.*, *48*, 1108–1113, doi:10.1016/j.asr.2011.05.024.

Wolff, R. S., B. E. Goldstein, and C. M. Yeates (1980), The onset and development of Kelvin-Helmholtz instability at the Venus ionopause, *J. Geophys. Res.*, *85*, 7697–7707, doi:10.1029/JA085iA13p07697.

Wu, Z. (1987), Calculation of the shape of the contact surface at Comet Halley, in *Diversity and Similarity of Comets*, edited by E. J. Rolfe and B. Battrick, *Eur. Space Agency Spec. Publ., ESA SP-278*, 69–73.